



UNIVERSITY OF LEEDS

This is a repository copy of *Experimental evidence for wall-rock pulverization during dynamic rupture at ultra-high pressure conditions*.

White Rose Research Online URL for this paper:
<http://eprints.whiterose.ac.uk/157637/>

Version: Accepted Version

Article:

Incel, S, Schubnel, A, Renner, J et al. (7 more authors) (2019) Experimental evidence for wall-rock pulverization during dynamic rupture at ultra-high pressure conditions. *Earth and Planetary Science Letters*, 528. 115832. ISSN 0012-821X

<https://doi.org/10.1016/j.epsl.2019.115832>

© 2019, Elsevier. This manuscript version is made available under the CC-BY-NC-ND 4.0 license <http://creativecommons.org/licenses/by-nc-nd/4.0/>.

Reuse

This article is distributed under the terms of the Creative Commons Attribution-NonCommercial-NoDerivs (CC BY-NC-ND) licence. This licence only allows you to download this work and share it with others as long as you credit the authors, but you can't change the article in any way or use it commercially. More information and the full terms of the licence here: <https://creativecommons.org/licenses/>

Takedown

If you consider content in White Rose Research Online to be in breach of UK law, please notify us by emailing eprints@whiterose.ac.uk including the URL of the record and the reason for the withdrawal request.



eprints@whiterose.ac.uk
<https://eprints.whiterose.ac.uk/>

1 **Experimental evidence for wall rock pulverization during dynamic rupture at ultra-high**
2 **pressure conditions**

3 Sarah Incel¹, Alexandre Schubnel², Jörg Renner³, Timm John⁴, Loïc Labrousse⁵, Nadège
4 Hilaiet⁶, Helen Freeman⁷, Yanbin Wang⁸, François Renard^{1,9}, and Bjørn Jamtveit¹

5
6 ¹Physics of Geological Processes, The Njord Centre, Department of Geosciences, University
7 of Oslo, Box 1048 Blindern, 0316 Oslo, Norway

8 ²Laboratoire de Géologie de l'ENS - PSL Research University - UMR8538 du CNRS, 24 Rue
9 Lhomond, 75005 Paris, France

10 ³Ruhr-Universität Bochum, Universitätsstraße 150, 44801 Bochum, Germany

11 ⁴Freie Universität Berlin, Institute of Geological Sciences, Malteserstr. 74-100, 12249 Berlin,
12 Germany

13 ⁵Sorbonne Université, CNRS-INSU, Institut des Sciences de la Terre Paris, IStEP, UMR
14 7193, 75005 Paris, France

15 ⁶Univ. Lille, CNRS, INRA, ENSCL, UMR 8207 - Unité Matériaux et Transformations,
16 59000 Lille, France

17 ⁷Helmholtz-Zentrum Potsdam, Deutsches GeoForschungsZentrum GFZ, Telegrafenberg,
18 14473 Potsdam, Germany

19 ⁸Center for Advanced Radiation Sources, the University of Chicago, Chicago, IL 60637, USA

20 ⁹Univ. Grenoble Alpes, Univ. Savoie Mont Blanc, CNRS, IRD, IFSTTAR,
21 ISTerre, 38000 Grenoble, France

22
23 *Correspondence to: sarah.incel@gmail.com

24 **Abstract**

25 The mechanisms triggering intermediate and deep earthquakes have puzzled geologists for
26 several decades. There is still no consensus concerning whether such earthquakes are triggered
27 by brittle or ductile mechanisms. We performed a deformation experiment on a synthetic
28 lawsonite-bearing blueschist at a confining pressure of 3 GPa and temperatures from 583 to
29 1,073 K. After deformation, the recovered sample reveals conjugated shear fractures. Garnet
30 crystals are dissected and displaced along these narrow faults and reveal micro- and
31 nanostructures that resemble natural pulverization structures as well as partial amorphization.
32 Formation of such structures is known to require strain rates exceeding 10^2 s^{-1} at low confining
33 pressures and is explained by the propagation of a dynamic shear rupture. The absence of
34 shearing in the pulverized wall rock is taken as evidence that these structures pre-date the
35 subsequent heat-producing frictional slip. In analogy to observations at low pressure we infer
36 that the garnet structures in our experiment result from rapid propagation of a shear fracture
37 even at the high pressure exerted on the sample and thus suggest that brittle deformation is
38 possible at lower crustal to upper mantle depths.

39

40 **Keywords:** pulverization, high-pressure deformation, dynamic rupture, lawsonite-blueschist,
41 DDIA apparatus, acoustic emissions

42 **1. Introduction**

43 During subduction at convergent plate margins, intermediate depth (70-300 km) and deep
44 (>300 km) earthquakes are common. Yet, the processes triggering earthquakes at the high
45 pressures (>1 GPa) prevailing at these depths are poorly understood. Both brittle (Raleigh and
46 Paterson, 1965; Kirby, 1987; Green II and Burnley, 1989; Dobson et al., 2002; Hacker et al.,

47 2003b; Schubnel et al., 2013; Okazaki and Hirth, 2016; Ferrand et al., 2017; Gasc et al., 2017;
48 Incel et al., 2017, 2019; and references therein) and ductile (Braeck and Podladchikov, 2007;
49 Kelemen and Hirth, 2007; John et al., 2009; Thielmann et al., 2015; Poli and Prieto, 2016; Prieto
50 et al., 2017; and references therein) mechanisms have been proposed.

51 While the suggested ductile mechanisms involve self-localizing failure by dissipative
52 heating and thermal runaway situations, the considered brittle mechanisms involve dynamic
53 rupture. In the former case, one expects significant shear deformation prior to seismic slip,
54 whereas in the latter case, wall rock damage may occur due to high strain rates and rapidly
55 changing stresses near a propagating rupture tip prior to frictional heating of the shear fracture
56 surfaces (Ben-Zion, 2003). Wall rock deformation associated with paleoearthquakes inferred
57 from the presence of pseudotachylytes, a rock type often assumed to be the result of frictional
58 melting and subsequent quenching (McKenzie and Brune, 1972; Sibson, 1975), was interpreted
59 as evidence for a thermal runaway mechanism (John et al., 2009; Deseta et al., 2014). Studies
60 of pseudotachylyte veins and their surrounding wall rocks in naturally deformed rocks do,
61 however, pose a number of challenges due to postseismic deformation and recovery processes
62 with respect to their formation (Guermani and Pennacchioni, 1998; Mancktelow, 2006;
63 Kirkpatrick and Rowe, 2013). Recent microstructural observations indicate extremely high
64 stresses in wall rocks around lower crustal earthquake zones, and abundant fragmentation
65 (Angiboust et al., 2012) without observable shear (Austrheim et al., 2017; Petley-Ragan et al.,
66 2018). Such fragmentation is often referred to as ‘pulverization’ when occurring around faults
67 in the shallow seismogenic regime and is assumed to result from dynamic rupture processes
68 (Dor et al., 2006; Mitchell and Faulkner, 2009; Rempe et al., 2013).

69 In a previous experimental study, synthetic polycrystalline lawsonite-bearing blueschist
70 samples were deformed at confining pressures corresponding to lower crustal to upper mantle
71 depths (Incel et al. 2017). Faulting was accompanied by the record of acoustic emissions and

72 the growth of eclogite-facies minerals monitored using in-situ powder diffraction. Examination
73 of the recovered run products revealed several conjugated faults decorated with nanocrystalline
74 eclogite-facies transformation products in samples that entered the stability field of eclogite.
75 Therefore, Incel et al. (2017) suggested that failure occurred due to transformation-induced
76 instabilities, a mechanism titled transformational faulting (see also Kirby, 1987; Green II and
77 Burnley, 1989). In one of these samples (BS_3_1073 in Incel et al. 2017), garnet grains that are
78 cut and displaced by the faults show microstructures similar to what has been described from
79 ‘pulverized’ garnets in natural fault rocks from lower crustal lithologies (Austrheim et al., 2017;
80 Petley-Ragan et al., 2018). Here, we further investigate the micro- and nanostructure of
81 different garnets found in this sample. In addition, we model the spatial relation of the
82 occurrence and absence of garnet fracturing relying on linear elastic fracture mechanics with
83 the aim to gain further insight into the nucleation and failure mechanisms of intermediate-depth
84 earthquakes.

85 **2. Experimental methods and analytical techniques**

86 2.1 Sample description and preparation of the starting material

87 A lawsonite-bearing blueschist from Alpine Corsica served as sample material. To avoid any
88 initial texture of the starting material a chemically homogeneous part of this blueschist was
89 crushed and sieved to a grain size $<38\ \mu\text{m}$. The major phases are glaucophane and lawsonite in
90 a ratio of ~3:2 making up ~90 vol.% of the powder. Minor and accessory phases are garnet,
91 omphacite, actinolite, titanite, and phengite. The blueschist powder was hot-pressed at 3 GPa
92 and 923 K for 24 hours in a piston-cylinder and machined to approx. 2.1 mm in diameter and 3
93 mm in height. After hot-pressing, the sample’s phases reveal a homogeneous texture (Fig. 1a).
94 In particular, the garnets are randomly distributed throughout the sample as evidenced by the
95 Mn-element distribution map (Fig. 1b).

96 2.2 D-DIA deformation experiment

97 A 9×9×8 mm sized amorphous Boron-epoxy cuboid was used as pressure medium for the
98 experiment performed using a D-DIA apparatus. The hot-pressed sample is located in the
99 middle of this cuboid, sandwiched between two gold foils and two alumina pistons, and
100 surrounded by a BN sleeve that is inserted into a graphite furnace.

101 The deformation apparatus is mounted on the GSECARS beamline at the Advanced Photon
102 Source, National Laboratory, Argonne, IL, USA. The use of synchrotron radiation during
103 deformation made it possible to calculate the differential stress as well as the strain and the
104 strain rate during deformation. Stress was calculated on lattice planes of glaucophane using
105 powder diffraction patterns that were taken every five minutes of the deforming sample and the
106 strain was measured by using radiographs of the sample that were also taken every five minutes
107 during deformation. Details of the stress and strain calculation are described by Incel et al.
108 (2017). Additionally, the D-DIA apparatus is equipped with an acoustic emission (AE) system.
109 Acoustic emissions were recorded using a sampling rate of 50 MHz and in trigger mode with a
110 trigger threshold of 250 mV on two channels. The duration of the largest AEs recorded were in
111 the range of a few hundred microseconds. Hence, the interval size over which the stress
112 measurements are made is around six magnitudes larger than the event duration. Further details
113 on the experimental and AE setup can be found in Wang et al. (2003), Gasc et al. (2011), and
114 Schubnel et al. (2013).

115 First, the sample assembly was loaded hydrostatically to a confining pressure (P_c) of 3 GPa
116 (here confining pressure P_c equals the least principal stress σ_3). Then, heating was initialized
117 by increasing the furnace power manually to reach a temperature of 583 K. The sample was
118 kept at these conditions for 30 min before deformation with a strain rate of approx. $5 \times 10^{-5} \text{ s}^{-1}$
119 commenced. While deformation of the sample proceeded, the power was increased in 10 W

120 steps to heat up the sample from initially 583 to 1073 K. Heating steps were initiated at 5, 12,
121 18, 20, 25, 30, and 35 % axial strain.

122 2.3 Analytical techniques

123 Microstructural analyses of the recovered sample were performed using a field-emission
124 scanning electron microscope (FE-SEM) with an acceleration voltage of 15 kV. To investigate
125 the nanostructure of this sample, three focused-ion beam (FIB) sections were cut using a FEI-
126 Helios G4 UC-Dual Beam system for imaging, analysis and transmission electron microscopy
127 (TEM). The nanostructural analyses were conducted using a FEI Tecnai TEM and a Jeol JEM
128 2011 transmission electron microscope. For both machines, the acceleration voltage was 200
129 keV.

130 **3. Results**

131 3.1 Mechanical data and acoustic emissions

132 During the first stage of deformation at a temperature of 583 K, the sample was strained by
133 5 % and the differential stress increased towards a peak stress of approx. 3 GPa, i.e. the level
134 of the confining pressure (Fig. 2). The differential stress decreased continuously during
135 syndeformational heating of the sample. A total axial strain of 40 % was accumulated by the
136 time the temperature reached 1073 K. In total 10 acoustic emissions were recorded between 10
137 to 19 % axial strain. Two events recorded at around 12 % and at approx. 19 % axial strain,
138 respectively, were large events almost reaching voltage saturation of the recording system (5
139 V).

140 3.2 Microstructural analyses

141 Microstructural investigations using the field-emission scanning electron microscope (FE-
142 SEM) revealed faults oriented at an angle of around 45° to the direction of the axial stress σ_1
143 crosscutting the entire sample (Fig. 3a). It is possible that either some of the fault-filling
144 material (gouge) of the major faults was lost during sample preparation or the fault surfaces
145 were separated during decompression. However, some relicts of gouge material are preserved
146 at the fault borders. These relicts show holes after interaction with the electron beam of the
147 SEM, implying that this material is poorly crystalline (Fig. 3c).

148 Two different types of garnets can be identified in the deformed sample, (i) garnet crystals
149 that are dissected and displaced along narrow faults ($<1 \mu\text{m}$ wide; Figs. 3c; 4a-c) and (ii)
150 unsheared garnet grains situated at some distance to the nearest fault (~ 0.5 to 1.5 mm ; Figs. 3b,
151 4d, e). Two example sets of displaced garnet parts show apparent shear displacements of 42
152 and $58 \mu\text{m}$, respectively (Figs. 3c; 4a). Back-scattered electron (BSE) imaging reveals that the
153 displaced garnet halves are fragmented into pieces with diameters $<1 \mu\text{m}$ (Figs. 3d; 4b) and
154 some of them were dragged along during slip (red arrow in Fig. 3d). Garnet grains located
155 further away from the fractures do not seem to be fragmented at this magnification in the SEM
156 (Figs. 3b; 4d, e).

157 3.3 Nanostructural analyses

158 Transmission electron microscope (TEM) analyses were performed at three different sites
159 (Fig. 3b, c) to investigate the nanometer-scale structures of: (i) the fault-gouge of the narrow
160 fault dissecting and displacing a garnet crystal, (ii) a garnet crystal that is cut by this narrow
161 fault, hereafter referred to as damage-zone garnet, and (iii) a garnet crystal located at a minimum
162 of $\sim 0.5 \text{ mm}$ from any fault, denoted as host-rock garnet. The fault-gouge contains garnet
163 crystals with sizes ranging from $<20 \text{ nm}$ to $\sim 100 \text{ nm}$. In bright field mode TEM images, the

164 material embedding the garnets appeared brighter than the garnet grains (Fig. 5a). An electron
165 diffraction pattern of this area showed a few diffraction spots but also a diffuse halo (Fig. 5b)
166 implying a combination of domains that have lost their long-range crystalline order and crystals
167 large enough to produce diffraction spots.

168 Scanning transmission electron microscopy (STEM) of the damage-zone garnet
169 demonstrates that this grain is completely shattered into small fragments (Figs. 5c, 6a)
170 surrounded by a fault-filling material exhibiting vesicles and idiomorphic crystals (Fig. 6a).
171 Using energy-dispersive spectroscopy (EDS) measurements these idiomorphic crystals were
172 identified as omphacite. The surrounding matrix mainly consists of Si, Al, Na, and Ca in
173 addition to O. The diffraction pattern obtained from a circular area with a diameter of ~500 nm
174 in the shattered damage-zone garnet shows few large and several weak diffraction spots,
175 indicative of a polycrystalline material, together with a diffuse halo in its center (Fig. 5c, d).
176 This halo is less prominent than the one obtained from diffraction of the fault-gouge (Fig. 5b).
177 A bright field and a dark field mode image of the same area within the shattered damage-zone
178 garnet taken at high magnification document grain-size and crystal-orientation variation,
179 respectively (Fig. 6b, c). The bright field image shows several grains ranging in size from ~10
180 to ~50 nm in diameter (Fig. 6b). A quantitative determination of the grain-size distribution is
181 hampered by the abundant overlap of small grains. Lattice fringes are clearly visible locally
182 (Fig. 6c). However, the brightness variation in the corresponding dark-field mode image
183 suggests variable lattice orientation on the nanometer scale.

184 Nanostructural analysis of the host-rock garnet shows numerous fracture-like features and
185 possibly subgrains ranging in diameter from several hundred nanometers to ~5 μm (Fig. 5e). In
186 contrast to the damage-zone garnet, though, very few grains have diameters <100 nm (Fig. 5c,
187 e). A diffraction pattern of an area with a diameter of ~500 nm (Fig. 5e) indicates a high degree
188 of crystallinity in this zone (Fig. 5f).

189 4. Discussion

190 4.1 Garnet pulverization due to dynamic rupture propagation

191 Our microscopic analyses revealed extensive fragmentation and grain-size reduction of the
192 damage-zone garnet. Its diffraction pattern shows numerous weak diffraction spots indicating
193 the presence of many small crystals. Additionally, a diffuse halo is observed implying that some
194 subdomains are either amorphous or too small (<10 nm) to produce well-defined diffraction
195 spots (Fig. 6c; Yund et al., 1990). On the contrary, the host-rock garnet is fully crystalline and
196 mainly reveals subgrain-formation (Fig. 5e, f). These experimental microstructures are
197 strikingly similar to what Austrheim et al. (2017) described as “pulverization structures” in
198 garnets found in close vicinity to a pseudotachylyte produced during coseismic loading and
199 faulting of granulites from the Bergen Arcs, Norway, and to those found in garnets from
200 mylonitic micaschists in the Sesia Zone, Swiss Alps (Trepmann and Stöckhert, 2002).

201 Based on the record of acoustic emissions (Fig. 2), faulting and associated pulverization of
202 the wall rock occurred at a confining pressure of ~3 GPa, a differential stress of ~2.5 GPa, in a
203 temperature range from 640 to 720 K, at an experimentally imposed strain rate of $5 \times 10^{-5} \text{ s}^{-1}$ and
204 at ~10 to 19 % axial strain. One characteristic feature of pulverized structures is the absence or
205 the low amount of shearing of the fragments (Trepmann and Stöckhert, 2002; Austrheim et al.,
206 2017). Due to the small fragment sizes of the damage-zone garnet it was not possible to measure
207 their orientation. It is likely that the fragments experienced some shearing during further
208 deformation as evidenced by the ‘tailing’ of the damage-zone garnet into the fault (red arrow
209 in Fig. 3d). However, because the fragments’ arrangement still mimics a typical garnet crystal
210 shape we can exclude significant shearing of the bulk crystals and their environment (Figs. 3c,
211 4a, 5c). As evidenced by the microstructure of the recovered sample showing lawsonite
212 pseudomorphs as well as by in-situ monitoring of the mineral assemblage during deformation,

213 extensive reaction comprising the dehydration of lawsonite took place at a later stage during
214 deformation (Incel et al., 2017). Therefore, most of the remaining strain was accommodated by
215 lawsonite dehydration involving a solid volume change of around -20 %.

216 When occurring at upper crustal depth (<15 km), wall-rock damage is explained by high
217 strain rates and stresses around a dynamically propagating rupture tip (Reches and Dewers,
218 2005; Dor et al., 2006; Doan and Gary, 2009; Mitchell et al., 2011; Bhat et al., 2012; Rempe et
219 al., 2013; Aben et al., 2017a, 2017b, 2016; Xu and Ben-Zion, 2017; Griffith et al., 2018). Due
220 to the much lower strength of rocks in tension than in compression, recently published studies
221 highlight the impact of isotropic or quasi-isotropic tension on the pulverization of rocks (Xu
222 and Ben-Zion, 2017; Griffith et al., 2018). In the model of Grady (1982) the author quantifies
223 the relation between the energy needed to create new fracture surfaces during fragmentation
224 and the inertial or kinetic energy available due to rapid loading. Later Glenn and Chudnovsky
225 (1986) added a strain energy term to this model that accounts for the energy consumed by the
226 solid until reaching its tensile strength. Based on this model, fragment size will not vary over a
227 wide range of strain rates (strain energy dominated regime). Once the tensile strength of the
228 material is exceeded, the fragment size exponentially decays with increasing strain rate (kinetic
229 energy dominated; Grady, 1982). Across natural faults, this situation is realized in close
230 distance (~5 cm) to the fault plane where strain rates are expected to be high (Griffith et al.
231 2018). In the present study, we follow a similar approach as presented in Griffith et al. (2018)
232 in order to investigate, if the above model can explain the observed difference in fragmentation
233 intensity between the damage-zone and the host-rock garnet. First, we check if the calculated
234 fragment size matches our measured garnet fragments using the Glenn and Chudnovsky (1986)
235 model. Then, we test if the corresponding strain rates fit the predicted strain rates around a
236 dynamically propagating mode II crack tip at the respective positions of the damage-zone and
237 the host-rock garnet using linear elastic fracture mechanics (see Freund, 1990). For these

238 calculations, we used a density $\rho = 3,000 \text{ kg m}^{-3}$, a garnet fracture toughness $K_{IC} = 1.5 \text{ MPa}$
239 (Mezeix and Green, 2006), and a range in garnet tensile strength $\sigma^* = 433 \text{ MPa}$ to 4.3 GPa
240 deduced using reported single crystal or aggregate compressive strengths (Pardavi-Horváth,
241 1984; Kavner, 2007) assuming that the tensile strength of a solid is around a third of its
242 compressive strength. We used a shear modulus $\mu = 64 \text{ GPa}$ for glaucophane (Bezacier et al.,
243 2010), a Poisson's ratio $\nu = 0.22$ (Cao et al., 2013), and two different rupture velocities $v_r = 0.8c_s$
244 and $v_r = 0.9c_s$ with c_s being the shear wave speed. The microstructural observations indicate a
245 coseismic slip of a few tens of micrometer (Figures 3c; 4a) corresponding to a range in fracture
246 energy G_c of ~ 0.1 to 100 J m^{-2} (Passelègue et al., 2016), deduced from experiments accounting
247 for the uncertainty regarding the critical slip distance (further explanations in Passelègue et al.,
248 2016).

249 The calculated fragment size distribution matches quite well the measured garnet fragments
250 of the host-rock and the damage-zone garnet, respectively (Figures 5; 7a). Based on linear
251 elastic fracture mechanics, strain rates at the position of the host-rock garnet range from $\sim 10^2$
252 to $\sim 10^4 \text{ s}^{-1}$ (Figure 7b). Combining the results of both calculations, the host-rock garnet plots
253 within the strain energy dominated regime (Figure 7). This fits well the nanostructural analysis
254 that reveals some fracture-like features, but mostly polygons that are homogeneously sized
255 resembling subgrains (Figures 5e; 8b). To explain the extensive fragmentation of the damage-
256 zone garnet, strain rates must have been high enough to exceed garnet's tensile strength. Based
257 on the measured fragment sizes of the damage-zone garnet, strain rates have to be at least 10^8
258 s^{-1} (Figure 7a). Since the crack tip passed through this garnet crystal, such high strain rates are
259 realized within the damage-zone garnet volume in close vicinity to the rupture tip (Figures 7b;
260 8a, b).

261 The theory of linear elastic fracture mechanics provides an asymptotic solution for a semi-
262 infinite crack that is only valid in the near-tip field (Freund, 1990). This requirement is

263 obviously difficult to satisfy regarding the length ratio of the shear fracture relative to the
 264 respective garnet distances to the fault plane. A previous theoretical study on the relation
 265 between wall-rock damage and depth reports an increase in the amount of fracture energy
 266 dissipated in the off-fault medium with increasing depth (Okubo et al., 2019). The authors also
 267 state that the width of the damage-zone decreases with depth. Consequently, this implies that
 268 at deeper depth the off-fault damage will be confined to a narrow zone around the fault.
 269 Showing extensively damaged garnets only in close vicinity to the fault, our experimental study
 270 confirms these theoretical results.

271 4.2 Frictional melting of blueschist

272 Sliding of the fracture surfaces in mode II causes a temperature increase, which may
 273 eventually lead to melting of the fracture surfaces. We deduce the presence of a solidified melt
 274 from the amorphous material present in the fault-filling material (Fig. 5a,b) and in some places
 275 intruded the shattered damage-zone garnet (Fig. 6a). In this “melting scenario”, the vesicles in
 276 the amorphous material reflect fluid exsolution during decompression of the melt and the
 277 observed idiomorphic omphacite crystals nucleate and grow during cooling of the melt (Fig.
 278 6a). Assuming a wet basalt solidus temperature T_s of ~1,000 K at ~3 GPa (Hacker et al., 2003a),
 279 a sliding-related increase in temperature of 280-360 K over the temperatures prevailing during
 280 the AE activity (640-720 K) would be sufficient to cause local melting. After Cardwell et al.
 281 (1978), the temperature rise ΔT on a slipping fault can be expressed as

$$282 \quad \Delta T = \frac{\tau D}{\rho c_p \sqrt{\pi \kappa t_{\text{slip}}}} \quad (\text{eq. 1})$$

283 with shear stress τ , shear displacement D , density ρ , specific heat capacity c_p (1,100 J kg⁻¹ K⁻¹
 284 at ~1,000 K; Hartlieb et al., 2016), thermal diffusivity κ (~10⁻⁶ m s⁻¹), and slip duration t_{slip} .
 285 The nominal shear stress τ and normal stress σ_n acting on the fault are ~1.25 GPa and 4.25 GPa,
 286 respectively (with $\theta \approx 45^\circ$, $\sigma_1 = 5.5$ GPa, and $\sigma_3 = 3$ GPa). Assuming a minimum total

287 displacement $D= 42 \mu\text{m}$ (Figs. 3c) and only 10 % of that slip to have happened coseismically
288 and a sliding velocity of $\sim 1 \text{ m s}^{-1}$ (for a crack-like rupture; Schubnel et al., 2013) gives a slip
289 duration t_{slip} of $\sim 4.2 \times 10^{-6} \text{ s}$. These estimates result in a ΔT of $>390 \text{ K}$ indeed exceeding the
290 difference between prevailing assembly temperature and the sample's solidus temperature.

291 The presence of a melt film on the fault surfaces can lead to fault lubrication (Di Toro et al.,
292 2006). Dynamic shear strength τ_f of a fault with a continuous melt film strongly depends on the
293 ratio between the width w of the molten zone that is filling the fault plane and the slip
294 displacement (e.g., Ferrand et al., 2018)

$$295 \quad \tau_f = \frac{\rho[H+c_p\Delta T]w}{(1-\eta)D} \quad (\text{eq. 2})$$

296 with the latent heat of fusion H ($\approx 3 \times 10^5 \text{ J K}^{-1}$) and the radiative efficiency η . In our sample,
297 the narrow fault that contains molten material shows a width of $w \approx 100\text{-}500 \text{ nm}$. Previous
298 studies showed that the seismic efficiency, as function of the mechanical energy spent on slip
299 during rupture, ranges between $0.1 < \eta < 0.5$ (Poli and Prieto, 2016). Within this span, equation
300 (2) gives a dynamic shear strength of the fault as low as ~ 7 to 66 MPa (Fig. 9a) corresponding
301 to friction coefficients of ~ 0.002 to 0.015 (Fig. 9b), i.e., significant lubrication (Figure 8c).

302 **5. Conclusion and implications**

303 The micro- and nanostructures observed in the damage-zone garnet, which resemble
304 pulverization structures in natural rocks at upper as well as at lower crustal depths, can be
305 explained by extensive fragmentation due to high strain rates associated with a dynamically
306 propagating shear fracture. Such microstructures are not, however, compatible with fault
307 models that involve failure by self-localizing thermal runaway mechanisms. In such a situation,
308 one would expect to see evidence of pre-failure shear strain in the wall rocks, and the local
309 differential stress levels should not rise above the initial externally imposed far-field stress

310 (John et al., 2009). However, it has been demonstrated that high local stresses, e.g., due to
311 coseismic loading, are required to fracture garnet (Trepmann and Stöckhert, 2002). After the
312 passage of the crack tip, frictional sliding of the fault surfaces causes melting and fault
313 lubrication. Our experimental study emphasizes the importance of dynamic rupture as a brittle
314 precursor to unstable frictional slip even at upper mantle depths.

315 **Acknowledgements**

316 The authors thank the two reviewers Greg Hirth and Ashley Griffith for their comments and
317 suggestions that helped improving the manuscript. The authors also thank Anja Schreiber for
318 the preparation of the FIB sections and Christian Chopin who provided the blueschist sample.
319 Special thanks to Frans Aben, François Passelègue, and Yehuda Ben-Zion for their help and
320 discussions and to Paul Meakin for a careful review of an early version of the manuscript. The
321 study received funding from the Alexander von Humboldt-foundation (Feodor Lynen-
322 fellowship to S.I.) and support from Geo.X in form of a travel Grant (to S.I.). Further funding
323 came from the People Program (Marie Curie Actions) of the European Union's Seventh
324 Framework Program FP7/2017-2013/ and Horizon 2020 under REA grant agreements n°
325 604713 (to A.S.) and n° 669972 (to B.J.), EAR-1661489 for the development of AE
326 experiments (Y.W.). This research used resources of the Advanced Photon Source, a U.S.
327 Department of Energy Office of Science User Facility operated by Argonne National
328 Laboratory (contract n° DE-AC02-06CH11357). Financial support for H.M.F through
329 funding provided by the German Helmholtz Recruiting Initiative (award number I-044-16-01)
330 to Liane G. Benning from the GFZ is acknowledged.

331 **References**

- 332 Aben, F.M., Doan, M., Mitchell, T.M., Toussaint, R., Reuschlé, T., Fondriest, M., Gratier, J.,
333 Renard, F., 2016. Dynamic fracturing by successive coseismic loadings leads to
334 pulverization in active fault zones 121, 2338–2360. doi:10.1002/2015JB012542
- 335 Aben, F.M., Doan, M.L., Gratier, J.P., Renard, F., 2017a. AGU Monograph - Fault Zone
336 Dynamic Processes: Evolution of Fault Properties During Seismic Rupture, 1st ed,
337 Current. John Wiley & Sons, Inc.
- 338 Aben, F.M., Doan, M.L., Gratier, J.P., Renard, F., 2017b. High strain rate deformation of porous
339 sandstone and the asymmetry of earthquake damage in shallow fault zones. Earth Planet.
340 Sci. Lett. 463, 81–91. doi:10.1016/j.epsl.2017.01.016
- 341 Angiboust, S., Agard, P., Yamato, P., Raimbourg, H., 2012. Eclogite breccias in a subducted
342 ophiolite: A record of intermediatedepth earthquakes? *Geology* 40, 707–710.
343 doi:10.1130/G32925.1
- 344 Austrheim, H., Dunkel, K.G., Plümper, O., Ildefonse, B., Liu, Y., Jamtveit, B., 2017.
345 Fragmentation of wall rock garnets during deep crustal earthquakes. *Sci. Adv.* 3, 1–7.
346 doi:10.1126/sciadv.1602067
- 347 Ben-Zion, Y., 2003. Appendix 2, Key Formulas in Earthquake Seismology. *Int. Handb. Earthq.*
348 *Eng. Seismol. Part B*, 1857–1875.
- 349 Bezacier, L., Reynard, B., Bass, J.D., Wang, J., Mainprice, D., 2010. Elasticity of glaucophane,
350 seismic velocities and anisotropy of the subducted oceanic crust. *Tectonophysics* 494,
351 201–210. doi:10.1016/j.tecto.2010.09.011
- 352 Bhat, H.S., Rosakis, A.J., Sammis, C.G., 2012. A Micromechanics Based Constitutive Model
353 for Brittle Failure at High Strain Rates. *J. Appl. Mech.* 79, 31016. doi:10.1115/1.4005897
- 354 Braeck, S., Podladchikov, Y.Y., 2007. Spontaneous thermal runaway as an ultimate failure
355 mechanism of materials. *Phys. Rev. Lett.* 98. doi:10.1103/PhysRevLett.98.095504

356 Cao, Y., Jung, H., Song, S., 2013. Petro-fabrics and seismic properties of blueschist and eclogite
357 in the North Qilian suture zone, NW China: Implications for the low-velocity upper layer
358 in subducting slab, trench-parallel seismic anisotropy, and eclogite detectability in the
359 subduction zone. *J. Geophys. Res. Solid Earth* 118, 3037–3058. doi:10.1002/jgrb.50212

360 Cardwell, R.K., Chinn, D.S., Moore, G.F., Turcotte, D.L., 1978. Frictional Heating on a Fault
361 Zone With Finite Thickness. *Geophys. J. R. Astron. Soc.* 52, 525–530. doi:10.1111/j.1365-
362 246X.1978.tb04247.x

363 Deseta, N., Ashwal, L.D., Andersen, T.B., 2014. Initiating intermediate-depth earthquakes:
364 Insights from a HP-LT ophiolite from Corsica. *Lithos* 206–207, 127–146.
365 doi:10.1016/j.lithos.2014.07.022

366 Di Toro, G., Hirose, T., Nielsen, S., Pennacchioni, G., Shimamoto, T., 2006. Natural and
367 Experimental Evidence During Earthquakes. *Science* (80-.). 311, 647–649.
368 doi:10.1126/science.1121012

369 Doan, M.L., Gary, G., 2009. Rock pulverization at high strain rate near the San Andreas fault.
370 *Nat. Geosci.* 2, 709–712. doi:10.1038/ngeo640

371 Dobson, D.P., Meredith, P.G., Boon, S.A., 2002. Simulation of subduction zone seismicity by
372 dehydration of serpentine. *Science* (80-.). 298, 1407–1410. doi:10.1126/science.1075390

373 Dor, O., Ben-Zion, Y., Rockwell, T.K., Brune, J., 2006. Pulverized rocks in the Mojave section
374 of the San Andreas Fault Zone. *Earth Planet. Sci. Lett.* 245, 642–654.
375 doi:10.1016/j.epsl.2006.03.034

376 Ferrand, T.P., Hilairet, N., Incel, S., Deldicque, D., Labrousse, L., Gasc, J., Renner, J., Wang,
377 Y., Green, H.W., Schubnel, A., 2017. Dehydration-driven stress transfer triggers
378 intermediate-depth earthquakes. *Nat. Commun.* 8, 1–11. doi:10.1038/ncomms15247

379 Ferrand, T.P., Labrousse, L., Eloy, G., Fabbri, O., Hilairet, N., Schubnel, A., 2018. Energy
380 balance from a mantle pseudotachylyte, Balmuccia, Italy. *J. Geophys. Res. Solid Earth.*

381 doi:10.1002/2017JB014795

382 Freund, L.B., 1990. *Dynamic Fracture Mechanics*, Cambridge University Press.

383 doi:10.1017/CBO9780511546761

384 Gasc, J., Hilaiet, N., Yu, T., Ferrand, T., Schubnel, A., Wang, Y., 2017. Faulting of natural
385 serpentinite: Implications for intermediate-depth seismicity. *Earth Planet. Sci. Lett.* 474,
386 138–147. doi:10.1016/j.epsl.2017.06.016

387 Gasc, J., Schubnel, A., Brunet, F., Guillon, S., Mueller, H.J., Lathe, C., 2011. Simultaneous
388 acoustic emissions monitoring and synchrotron X-ray diffraction at high pressure and
389 temperature: Calibration and application to serpentinite dehydration. *Phys. Earth Planet.*
390 *Inter.* 189, 121–133. doi:10.1016/j.pepi.2011.08.003

391 Glenn, L.A., Chudnovsky, A., 1986. Strain-energy effects on dynamic fragmentation. *J. Appl.*
392 *Phys.* 59, 1379–1380.

393 Grady, D.E., 1982. Local inertial effects in dynamic fragmentation. *J. Appl. Phys.* 53, 322–325.
394 doi:10.1063/1.329934

395 Green II, H.W., Burnley, P.C., 1989. A new self-organizing mechanism for deep-focus
396 earthquakes. *Nature* 341, 733–737. doi:10.1038/341733a0

397 Griffith, W.A., St. Julien, R.C., Ghaffari, H.O., Barber, T.J., 2018. A Tensile Origin for Fault
398 Rock Pulverization. *J. Geophys. Res. Solid Earth* 123, 7055–7073.
399 doi:10.1029/2018JB015786

400 Guermani, A., Pennacchioni, G., 1998. Brittle precursors of plastic deformation in a granite: an
401 example from the Mont Blanc massif (Helvetic, western Alps). *J. Struct. Geol.* 20, 135–
402 148. doi:10.1016/S0191-8141(97)00080-1

403 Hacker, B.R., Abers, G.A., Peacock, S.M., 2003a. Subduction factory 1. Theoretical
404 mineralogy, densities, seismic wave speeds, and H₂O contents. *J. Geophys. Res. Solid*
405 *Earth* 108, 1–26. doi:10.1029/2001JB001127

406 Hacker, B.R., Peacock, S.M., Abers, G.A., Holloway, S.D., 2003b. Subduction factory 2. Are
407 intermediate-depth earthquakes in subducting slabs linked to metamorphic dehydration
408 reactions? *J. Geophys. Res. Solid Earth* 108. doi:10.1029/2001JB001129

409 Hartlieb, P., Toifl, M., Kuchar, F., Meisels, R., Antretter, T., 2016. Thermo-physical properties
410 of selected hard rocks and their relation to microwave-assisted comminution. *Miner. Eng.*
411 91, 34–41. doi:10.1016/j.mineng.2015.11.008

412 Incel, S., Hilairet, N., Labrousse, L., John, T., Deldicque, D., Ferrand, T.P., Wang, Y., Morales,
413 L., Schubnel, A., 2017. Laboratory earthquakes triggered during eclogitization of
414 lawsonite-bearing blueschist. *Earth Planet. Sci. Lett.* 459, 320–331.
415 doi:10.1016/j.epsl.2016.11.047

416 Incel, S., Labrousse, L., Hilairet, N., John, T., Gasc, J., Shi, F., Wang, Y., Andersen, T.B.,
417 Renard, F., Jamtveit, B., Schubnel, A., 2019. Reaction-induced embrittlement of the lower
418 continental crust. *Geology* 47, 235–238. doi:https://doi.org/10.1130/G45527.1

419 John, T., Medvedev, S., Rüpke, L.H., Andersen, T.B., Podladchikov, Y.Y., Austrheim, H.,
420 2009. Generation of intermediate-depth earthquakes by self-localizing thermal runaway.
421 *Nat. Geosci.* 2, 137–140. doi:10.1038/ngeo419

422 Kavner, A., 2007. Garnet yield strength at high pressures and implications for upper mantle and
423 transition zone rheology. *J. Geophys. Res. Solid Earth* 112, 1–9.
424 doi:10.1029/2007JB004931

425 Kelemen, P.B., Hirth, G., 2007. A periodic shear-heating mechanism for intermediate-depth
426 earthquakes in the mantle. *Nature* 446, 787–790. doi:10.1038/nature05717

427 Kirby, S.H., 1987. Localized polymorphic phase transformations in high-pressure faults and
428 applications to the physical mechanism of deep earthquakes. *J. Geophys. Res. Solid Earth*
429 92, 13789–13800. doi:10.1029/JB092iB13p13789

430 Kirkpatrick, J.D., Rowe, C.D., 2013. Disappearing ink: How pseudotachylytes are lost from the

431 rock record. *J. Struct. Geol.* 52, 183–198. doi:10.1016/j.jsg.2013.03.003

432 Mancktelow, N.S., 2006. How ductile are ductile shear zones? *Geology* 34, 345–348.
433 doi:10.1130/G22260.1

434 McKenzie, D., Brune, J.N., 1972. Melting on Fault Planes During Large Earthquakes. *Geophys.*
435 *J. R. Astron. Soc.* 29, 65–78. doi:10.1111/j.1365-246X.1972.tb06152.x

436 Mezeix, L., Green, D.J., 2006. Comparison of the mechanical properties of single crystal and
437 polycrystalline yttrium aluminum garnet. *Int. J. Appl. Ceram. Technol.* 3, 166–176.
438 doi:10.1111/j.1744-7402.2006.02068.x

439 Mitchell, T.M., Ben-Zion, Y., Shimamoto, T., 2011. Pulverized fault rocks and damage
440 asymmetry along the Arima-Takatsuki Tectonic Line, Japan. *Earth Planet. Sci. Lett.* 308,
441 284–297. doi:10.1016/j.epsl.2011.04.023

442 Mitchell, T.M., Faulkner, D.R., 2009. The nature and origin of off-fault damage surrounding
443 strike-slip fault zones with a wide range of displacements: A field study from the Atacama
444 fault system, northern Chile. *J. Struct. Geol.* 31, 802–816. doi:10.1016/j.jsg.2009.05.002

445 Okazaki, K., Hirth, G., 2016. Dehydration of lawsonite could directly trigger earthquakes in
446 subducting oceanic crust. *Nature* 530, 81–84. doi:10.1038/nature16501

447 Okubo, K., Bhat, H.S., Rougier, E., Marty, S., Schubnel, A., Lei, Z., Knight, E.E., Klinger, Y.,
448 2019. Dynamics, radiation and overall energy budget of earthquake rupture with coseismic
449 off-fault damage. arXiv:1901.01771.

450 Pardavi-Horváth, M., 1984. Microhardness and brittle fracture of garnet single crystals. *J.*
451 *Mater. Sci.* 19, 1159–1170. doi:10.1007/BF01120025

452 Passelègue, F.X., Schubnel, A., Nielsen, S., Bhat, H.S., Deldicque, D., Madariaga, R., 2016.
453 Dynamic rupture processes inferred from laboratory microearthquakes. *J. Geophys. Res.*
454 *Solid Earth* 121, 4343–4365. doi:10.1002/2015JB012694

455 Petley-Ragan, A., Dunkel, K.G., Austrheim, H., Ildefonse, B., Jamtveit, B., 2018.

456 Microstructural Records of Earthquakes in the Lower Crust and Associated Fluid-Driven
457 Metamorphism in Plagioclase-Rich Granulites. *J. Geophys. Res. Solid Earth* 123, 3729–
458 3746. doi:10.1029/2017JB015348

459 Poli, P., Prieto, G.A., 2016. Global rupture parameters for deep and intermediate-depth
460 earthquakes. *J. Geophys. Res. Solid Earth* 121, 8871–8887. doi:10.1002/2016JB013521

461 Prieto, G.A., Froment, B., Yu, C., Poli, P., Abercrombie, R., 2017. Earthquake rupture below
462 the brittle-ductile transition in continental lithospheric mantle. *Sci. Adv.* 3, 1–6.
463 doi:10.1126/sciadv.1602642

464 Raleigh, C.B., Paterson, M.S., 1965. Experimental deformation of serpentinite and its tectonic
465 implications. *J. Geophys. Res.* 70, 3965–3985. doi:10.1029/JZ070i016p03965

466 Reches, Z., Dewers, T.A., 2005. Gouge formation by dynamic pulverization during earthquake
467 rupture. *Earth Planet. Sci. Lett.* 235, 361–374. doi:10.1016/j.epsl.2005.04.009

468 Rempe, M., Mitchell, T., Renner, J., Nippres, S., Ben-Zion, Y., Rockwell, T., 2013. Damage
469 and seismic velocity structure of pulverized rocks near the San Andreas Fault. *J. Geophys.*
470 *Res. Solid Earth* 118, 2813–2831. doi:10.1002/jgrb.50184

471 Schubnel, A., Brunet, F., Hilairet, N., Gasc, J., Wang, Y., Green, H.W., 2013. Deep-focus
472 earthquake analogs recorded at high pressure and temperature in the laboratory. *Science*
473 (80-.). 341, 1377–1380. doi:10.1126/science.1240206

474 Sibson, R.H., 1975. Generation of Pseudotachylyte by Ancient Seismic Faulting. *Geophys. J.*
475 *R. Astron. Soc.* 43, 775–794. doi:10.1111/j.1365-246X.1975.tb06195.x

476 Thielmann, M., Rozel, A., Kaus, B.J.P., Ricard, Y., 2015. Intermediate-depth earthquake
477 generation and shear zone formation caused by grain size reduction and shear heating.
478 *Geology* 43, 791–794. doi:10.1130/G36864.1

479 Trepmann, C.A., Stöckhert, B., 2002. Cataclastic deformation of garnet: A record of synseismic
480 loading and postseismic creep. *J. Struct. Geol.* 24, 1845–1856. doi:10.1016/S0191-

481 8141(02)00004-4

482 Wang, Y., Durham, W.B., Gettings, I.C., Weidner, D.J., 2003. The deformation-DIA: A new

483 apparatus for high temperature triaxial deformation to pressures up to 15 GPa. *Rev. Sci.*

484 *Instrum.* 74, 3002–3011. doi:10.1063/1.1570948

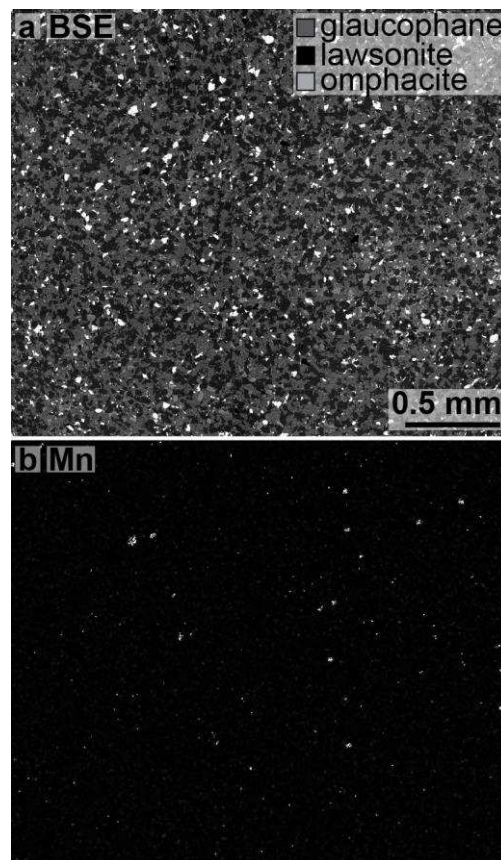
485 Xu, S., Ben-Zion, Y., 2017. Theoretical constraints on dynamic pulverization of fault zone

486 rocks. *Geophys. J. Int.* 209, 282–296. doi:10.1093/gji/ggx033

487 Yund, R.A., Blanpied, M.L., Tullis, T.E., Weeks, J.D., 1990. Amorphous Material in High

488 Strain Experimental Fault Gouges. *J. Geophys. Res.* 95, 15,589-15,602.

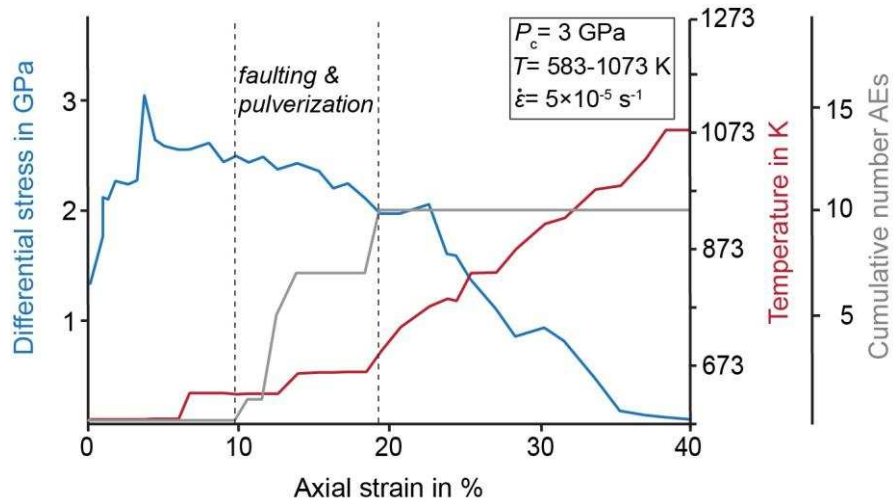
489



490

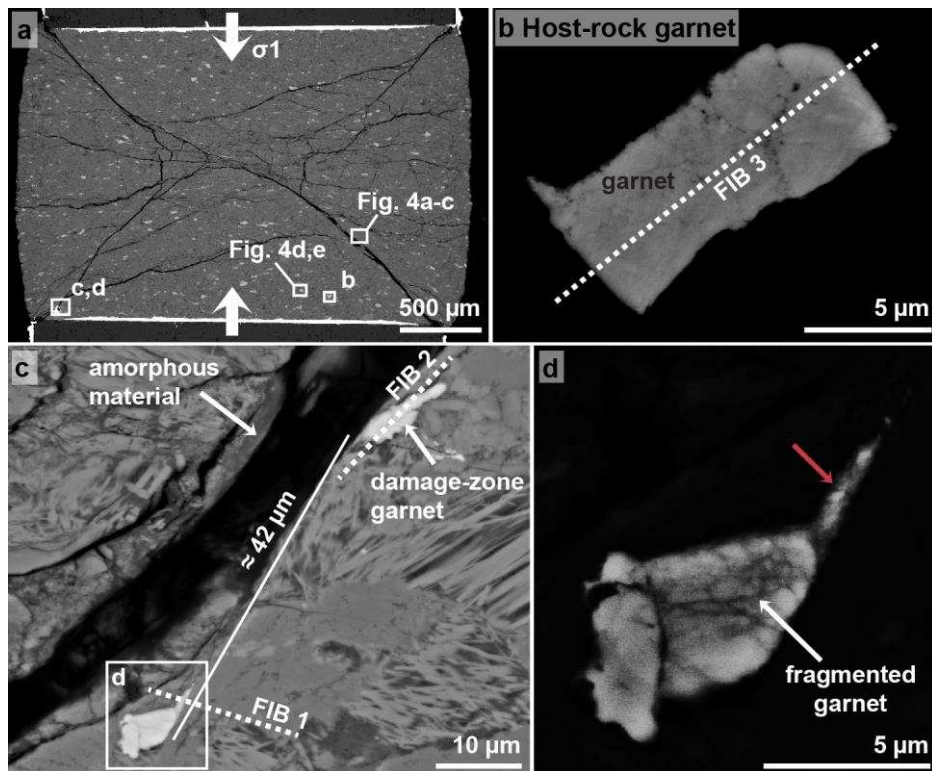
491 **Figure 1:** The starting material after hot-pressing. a) Backscattered electron (BSE) image
492 showing that the phases are homogeneously distributed throughout the sample. b) A Mn-
493 distribution map of the same region was used to highlight the location of garnet crystals.

494



495

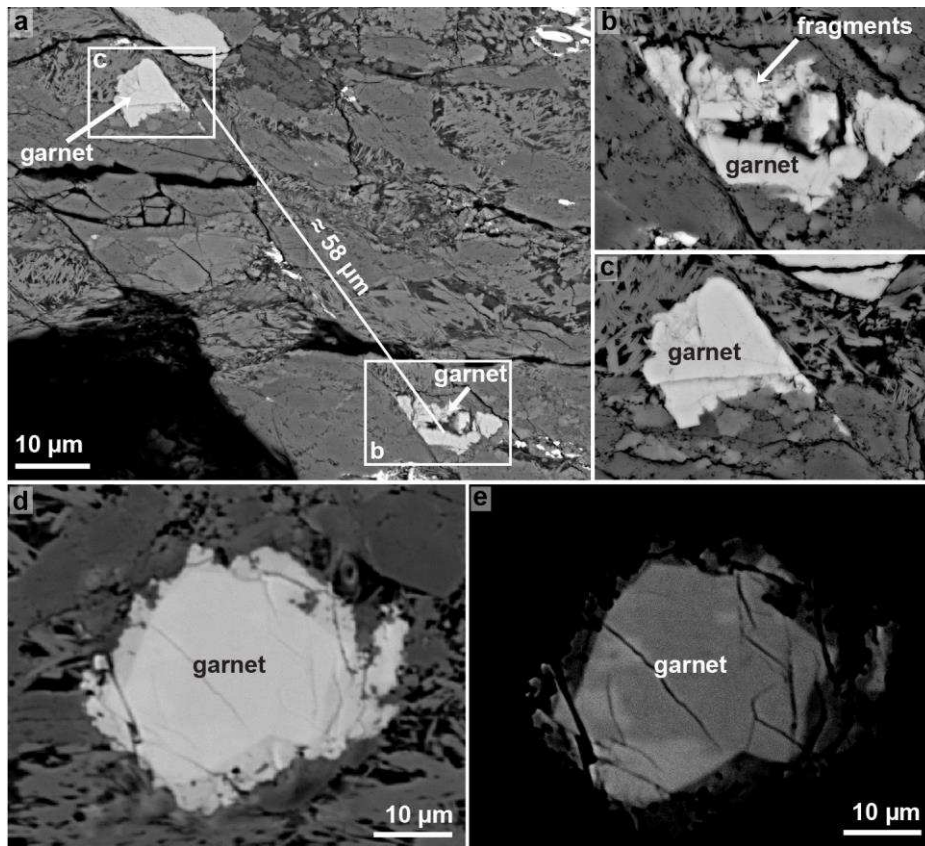
496 **Figure 2:** Differential stress, temperature, and cumulative number of acoustic emission (AE)
 497 events over axial strain. Based on the record of AEs (grey curve), faulting and pulverization
 498 occurs at a confining pressure (P_c)= 3 GPa, a differential stress of ~ 2.5 GPa (blue curve), in a
 499 temperature range of 640 to 720 K (red curve), at an imposed strain rate ($\dot{\epsilon}$) = $5 \times 10^{-5} \text{ s}^{-1}$, and an
 500 axial strain $\epsilon = \sim 10$ -19 %.
 501



502

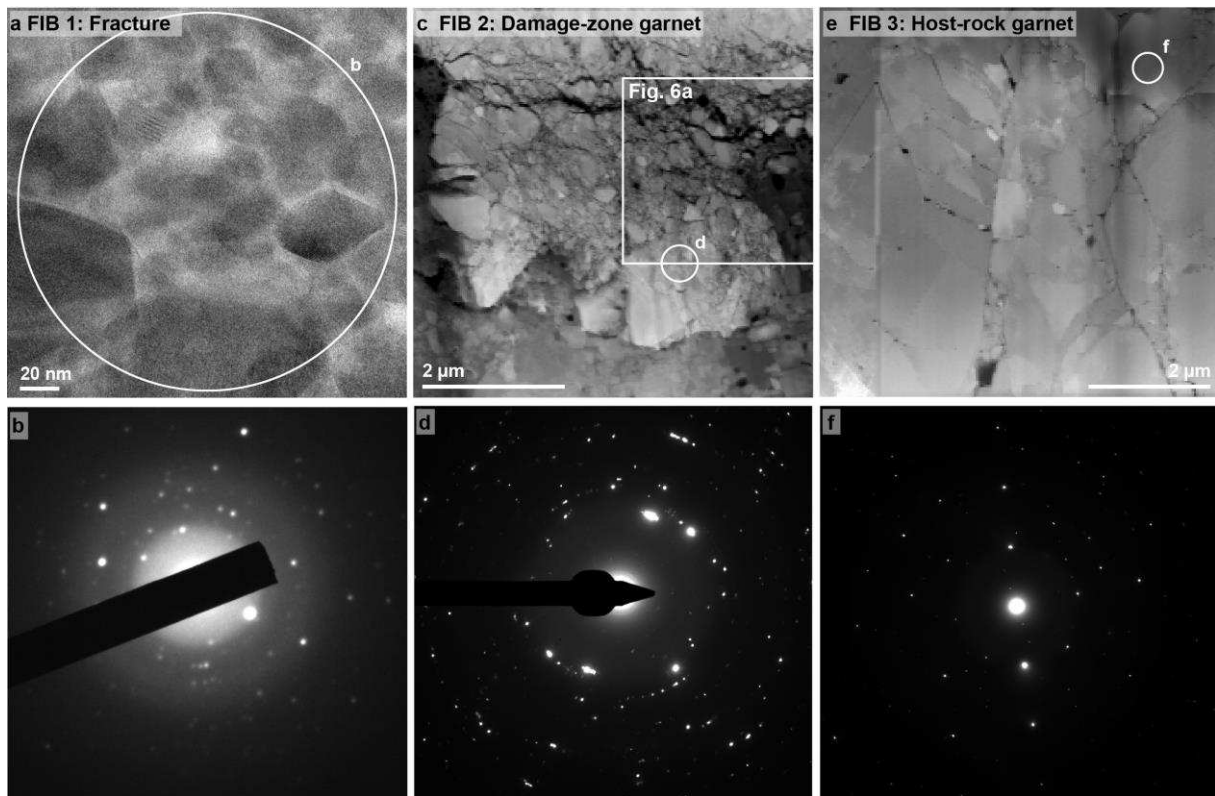
503 **Figure 3:** Backscattered electron images of the lawsonite-bearing blueschist sample after
 504 deformation. a) Overview image of the sample showing faults oriented at $\sim 45^\circ$ towards σ_1
 505 crosscutting the sample. The positions of the high-magnification images in b-d as well as the
 506 position for Fig. 4 are highlighted with white rectangles, respectively. b) The host-rock garnet
 507 crystal that is located at $\sim 0.5 \mu\text{m}$ to the closest fault. The location of FIB section 3 is shown as
 508 white dashed line. c) A garnet pair that is dissected and displaced along a narrow fault. The
 509 apparent displacement is $\sim 42 \mu\text{m}$. The locations for FIB sections 1 and 2 are marked by white

510 dashed lines. The white rectangle shows the location of a garnet half presented in d. d) At high
511 magnification and high brightness contrast the garnet half appears fragmented into several
512 pieces < 1 μ m.
513



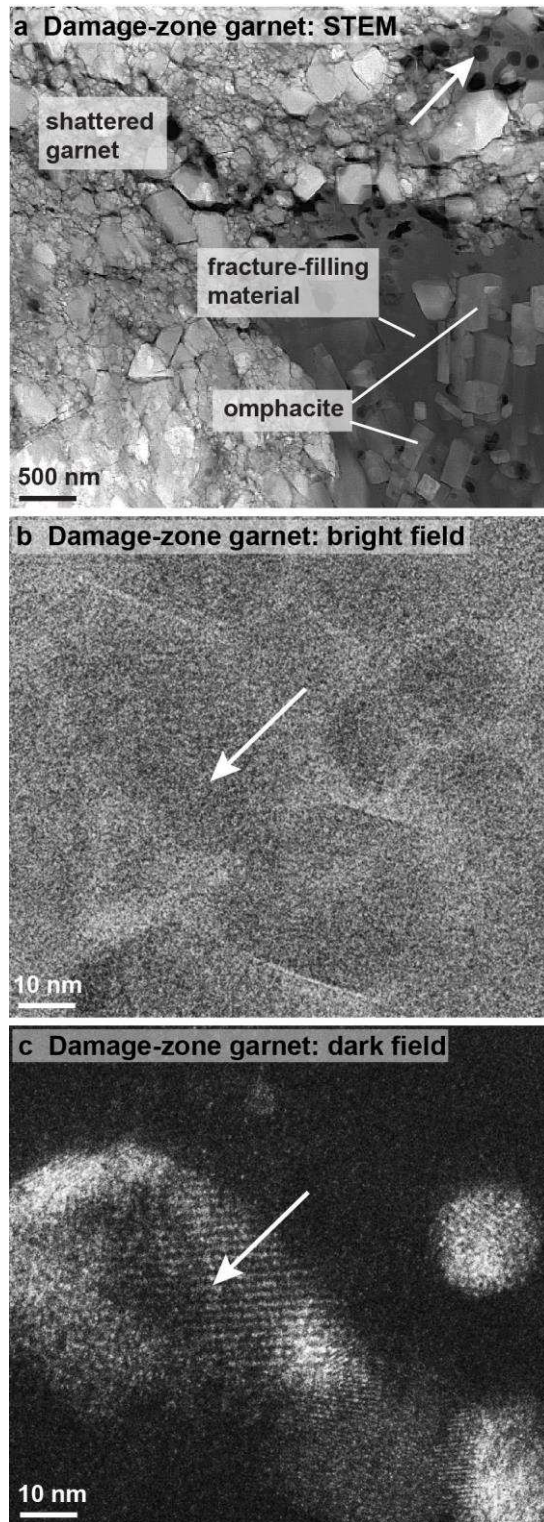
514

515 **Figure 4:** a) Backscattered electron images of another pair of dissected and displaced crystals
516 that are offset by a narrow fault. The offset along the narrow fault is ~58 μ m. b and c) The two
517 halves of the garnet pair showing extensive fragmentation in b). d and e) This garnet was found
518 at ~1 mm from the nearest fault and seems relatively intact. e) Same crystal as in d) with the
519 image taken at a higher brightness contrast at the SEM.
520



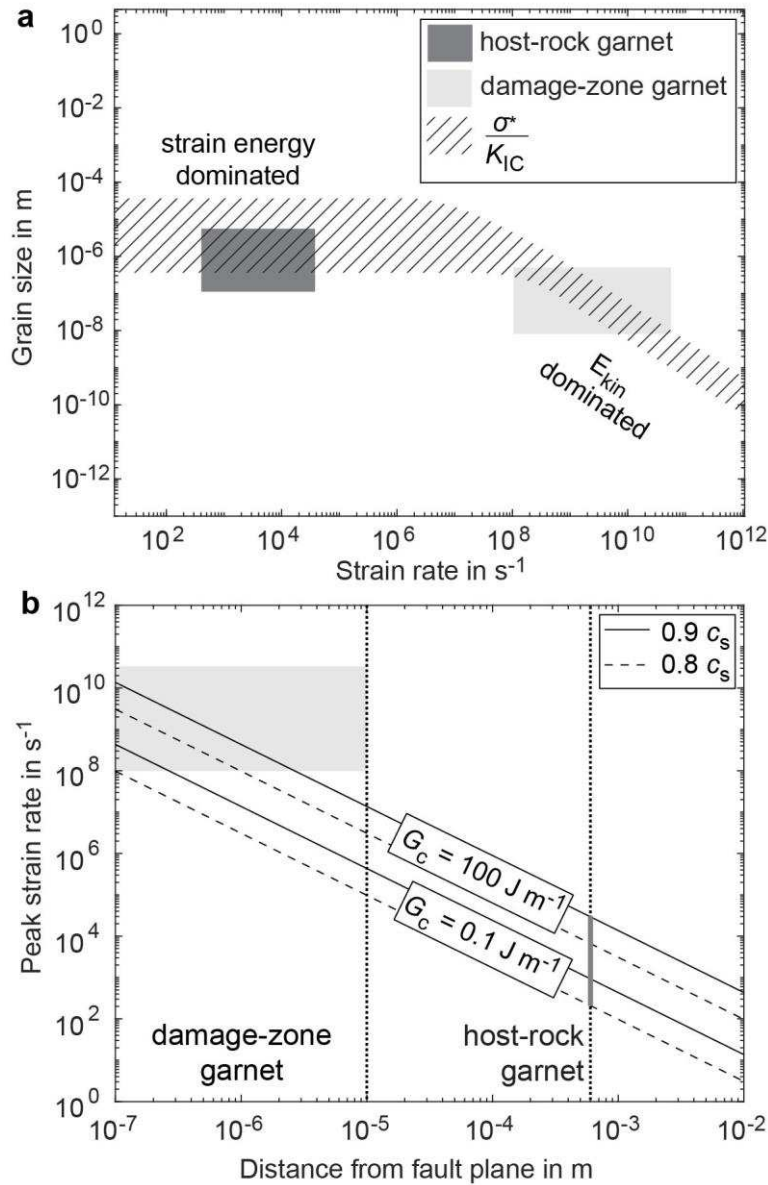
521

522 **Figure 5:** Transmission electron microscope images of the three FIB sections 1-3. a and b) FIB
 523 1 revealing the fault-filling material. a) Bright field image showing dark (i.e. crystalline) garnet
 524 crystals floating in a bright (i.e. amorphous) material. The location chosen for a diffraction
 525 pattern is highlighted by a white circle. b) Diffraction pattern of the fault-filling material
 526 exhibiting few large and several weak diffraction spots and a diffuse halo. c and d) FIB section
 527 2 cut across the damage-zone garnet next to the narrow fault. c) In STEM mode the damage-
 528 zone garnet appears to be completely shattered into pieces $<1 \mu\text{m}$. The white rectangle marks
 529 the position of Fig. 6a and the white circle shows the location of the diffraction pattern. d)
 530 Diffraction pattern of the shattered damage-zone garnet. Many weak diffraction spots indicate
 531 the presence of numerous small crystals. There is also a diffuse halo in the center of the
 532 diffraction pattern. e and f) FIB section 3 cut across the relatively intact host-rock garnet located
 533 at $\sim 0.5 \mu\text{m}$ from a fault. e) The fragments are much larger than those found in the damage-zone
 534 garnet. The white circle highlights the location chosen for a diffraction pattern. f) The
 535 diffraction pattern of the area shown in e) presents a crystalline structure.
 536



537

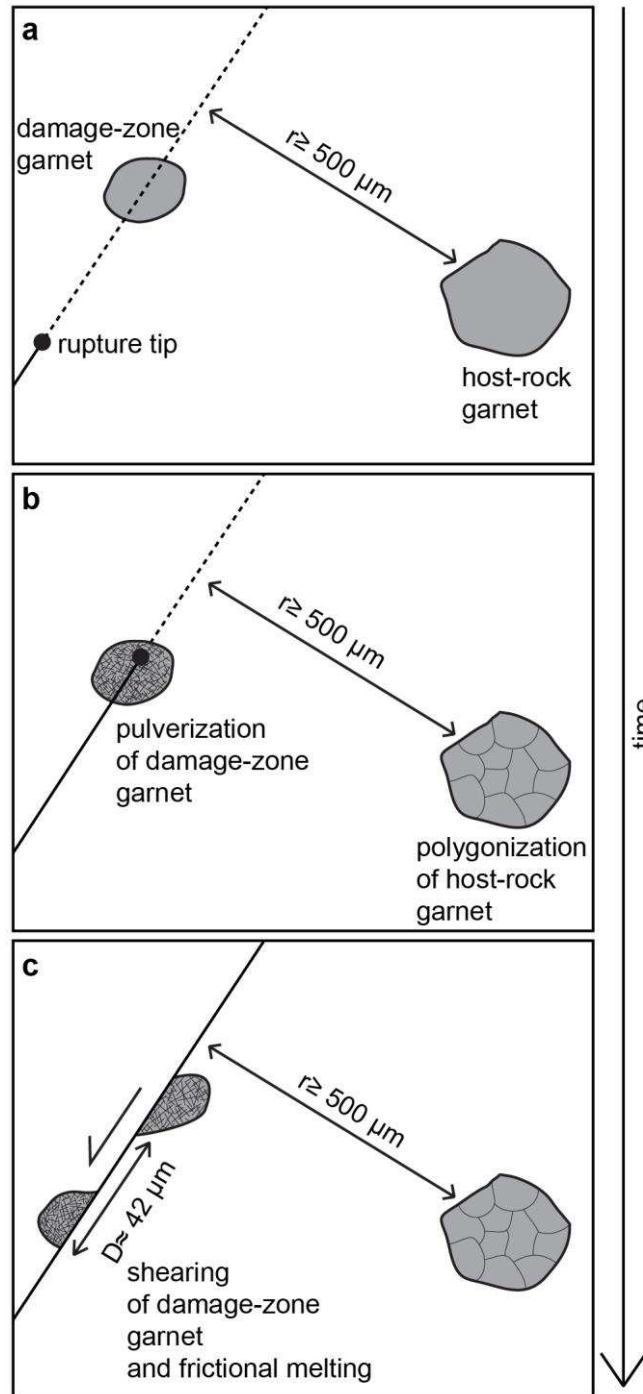
538 **Figure 6:** Transmission electron microscopy images of the shattered damage-zone garnet. a)
 539 STEM image revealing the fault-filling material surrounding the damage-zone garnet. Within
 540 this material vesicles (white arrow) and idiomorphic omphacite crystals can be found. b) Bright
 541 field image taken in the same zone as the diffraction pattern (Fig. 5c, d). c) The same area as
 542 shown in b) taken in dark field mode. The large grain marked by the white arrow shows
 543 subdomains (≤ 10 nm) that are slightly tilted.



544

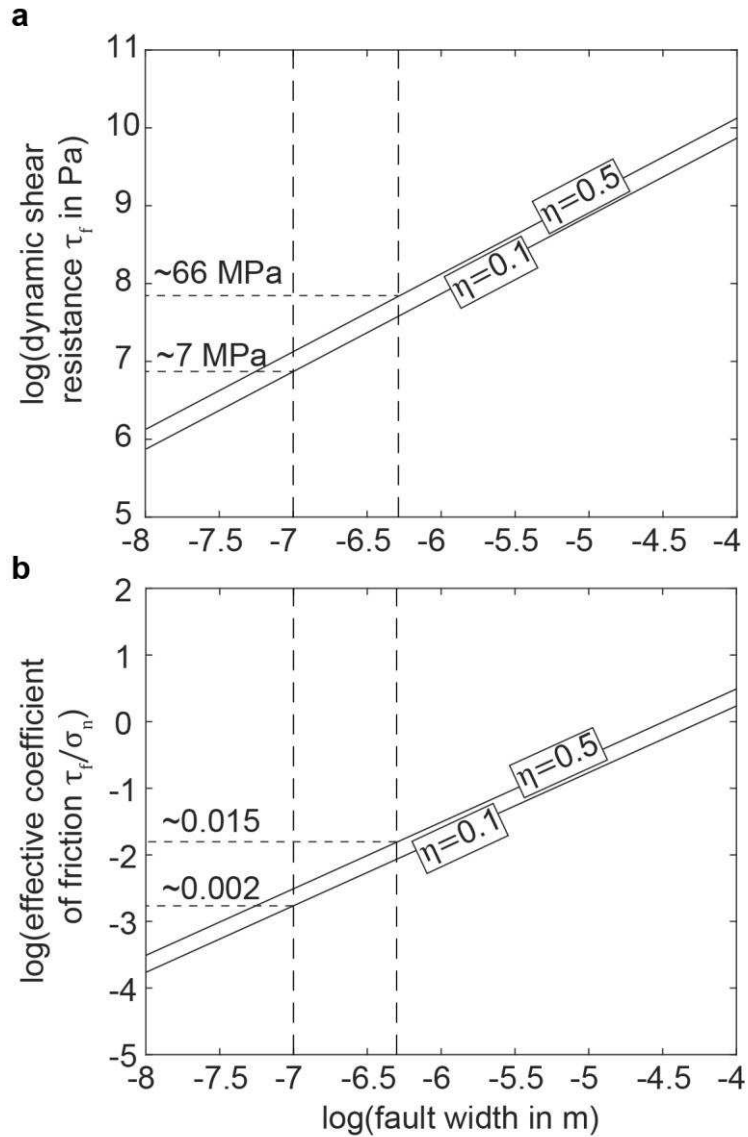
545 **Figure 7:** a) Grain size versus strain rate plot based on the models of Grady (1982) and Glenn
 546 and Chudnovsky (1986). The measured garnet fragments of the host-rock (dark grey rectangle)
 547 and the damage-zone garnet fragments (light grey rectangle) fit quite well the calculated
 548 fragment sizes (dashed area) over the investigated strain rate range. The minimum tensile
 549 strength for garnet aggregates is 433 MPa deduced from the compressive strength of garnet
 550 aggregates under confinement (Kavner, 2007). The maximum tensile strength was deduced
 551 from single crystal hardness measurements reported by Pardavi-Horváth (1984). For both we
 552 assumed that the tensile strength is around a third of the compressive strength. The fracture
 553 toughness of garnet is ~ 1.5 MPa (Mezeix and Green, 2006). b) Peak strain rates as a function
 554 of distance from the fault plane for two different rupture speeds v_r ($0.8c_s$ and $0.9c_s$) and two
 555 different fracture energies G_c (0.1 J m^{-1} and 100 J m^{-1} ; Passelègue et al., 2016).

556



557

558 **Figure 8:** a) Prior to rupture, both garnet crystals are intact. b) The rupture tip passes through
 559 the damage-zone garnet. Pulverization of the damage-zone garnet occurs due to the extreme
 560 strain rate around the crack tip (E_{kin} dominated Figure 7a). Because strain rate decays with
 561 distance, the host-rock garnet that is located at a minimum distance of $\sim 500 \mu\text{m}$ to the nearest
 562 fault only shows the formation of subgrains (strain energy dominated Figure 7a). c) Shearing
 563 behind the rupture tip causes the displacement of the garnet halves and eventually frictional
 564 melting of the fault surfaces.



565

566 **Figure 9:** a) Dynamic shear resistance and b) effective coefficient of friction versus width of
 567 the slip-associated melt layer. The vertical dashed lines mark the measured width of the molten
 568 zone filling out the fault along which a garnet pair is dissected and displaced (Fig. 3c). Recent
 569 studies show that the radiative efficiency increases with depth ranging between $\eta= 0.1$ to 0.5
 570 for intermediate depth earthquakes (50-300 km). The dashed horizontal lines indicate the
 571 intercept of this radiative efficiency range and the width range of the molten zone (~ 100 to 500
 572 nm) measured in the sample. The dynamic shear resistance would be ~ 7 to 66 MPa (a) resulting
 573 in an effective coefficient of friction of ~ 0.002 to 0.015 (b).